



**HAL**  
open science

# Chemistry and Mass Density of Aluminum Hydroxide Gel in Eco-Cements by Ptychographic X-ray Computed Tomography

Ana Cuesta, Angeles G de la Torre, Isabel Santacruz, Pavel Trtik, Julio Cesar da Silva, Ana Diaz, Mirko Holler, Miguel a G Aranda

► **To cite this version:**

Ana Cuesta, Angeles G de la Torre, Isabel Santacruz, Pavel Trtik, Julio Cesar da Silva, et al.. Chemistry and Mass Density of Aluminum Hydroxide Gel in Eco-Cements by Ptychographic X-ray Computed Tomography. *Journal of Physical Chemistry C*, 2017, 121, pp.3044 - 3054. 10.1021/acs.jpcc.6b10048 . hal-03751674

**HAL Id: hal-03751674**

**<https://hal.science/hal-03751674>**

Submitted on 15 Aug 2022

**HAL** is a multi-disciplinary open access archive for the deposit and dissemination of scientific research documents, whether they are published or not. The documents may come from teaching and research institutions in France or abroad, or from public or private research centers.

L'archive ouverte pluridisciplinaire **HAL**, est destinée au dépôt et à la diffusion de documents scientifiques de niveau recherche, publiés ou non, émanant des établissements d'enseignement et de recherche français ou étrangers, des laboratoires publics ou privés.

This document is the accepted manuscript version of the following article:  
Cuesta, A., De La Torre, A. G., Santacruz, I., Trtik, P., Da Silva, J. C., Diaz, A., ...  
Aranda, M. A. G. (2017). Chemistry and mass density of aluminum hydroxide gel in eco-  
cements by ptychographic X-ray computed tomography. *Journal of Physical Chemistry C*,  
121(5), 3044–3054. <https://doi.org/10.1021/acs.jpcc.6b10048>

## Chemistry and Mass Density of Aluminum Hydroxide Gel in Eco-Cements by Ptychographic X-ray Computed Tomography

Ana Cuesta<sup>†</sup>, Angeles G. De la Torre<sup>#</sup>, Isabel Santacruz<sup>#</sup>, Pavel Trtik<sup>§</sup>, Julio C. da Silva<sup>§§</sup>, Ana Diaz<sup>§</sup>,  
Mirko Holler<sup>§</sup>, Miguel A. G. Aranda<sup>†,\*</sup>

<sup>†</sup> ALBA Synchrotron, Carrer de la Llum 2-26, E-08290 Cerdanyola del Vallès, Barcelona, Spain

<sup>#</sup> Departamento de Química Inorgánica, Cristalografía y Mineralogía, Universidad de Málaga, 29071-Málaga, Spain

<sup>§</sup> Paul Scherrer Institut, Villigen PSI, 5232, Switzerland

\* To whom correspondence should be addressed.

<sup>§</sup> Currently at European Synchrotron Radiation Facility, Grenoble, 38000, France.

**ABSTRACT:** Eco-cements are a desirable alternative to ordinary Portland cements because of their lower CO<sub>2</sub> footprints. Some ye'elimate-based eco-cements are attracting a lot of interest. Understanding the reasons for the mechanical performances requires the characterization of features such as mass density of the hydrated component phases, including the amorphous gel, on the sub-micrometer scale which is challenging. Here we use ptychographic X-ray computed tomography to provide 3D mass density and attenuation coefficient distributions of eco-cement pastes with an isotropic resolution close to 100 nm allowing to distinguish between component phases with very similar contrast. In combination with laboratory techniques such as the Rietveld method, <sup>27</sup>Al MAS-NMR and electron microscopies, we report compositions and densities of key components. The ettringite and gel volume distributions have been mapped out in the segmented tomograms. Moreover, we discriminate between an aluminum hydroxide gel and calcium aluminum monosulfate, which have close electron density values. Specifically, the composition and mass density of two aluminum hydroxide gel agglomerates have been determined: (CaO)<sub>0.04</sub>Al(OH)<sub>3</sub>·2.3H<sub>2</sub>O with 1.48(3) g·cm<sup>-3</sup> and (CaO)<sub>0.12</sub>Al(OH)<sub>3</sub> with 2.05(3) g·cm<sup>-3</sup>, which was a long standing challenge.

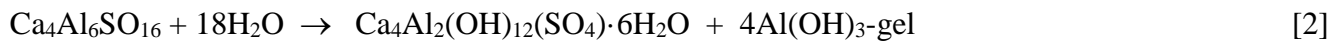
## INTRODUCTION

The world's yearly consumption of concrete is well over 6 km<sup>3</sup>, or more than 2.5 tonnes per person.<sup>1</sup> This is based mainly on ordinary Portland cements (OPCs). On average, for every ton of type-I OPC produced, 0.97 tonnes of CO<sub>2</sub> are released into the atmosphere, that includes the emissions derived from the burning of coal in the kiln and the electricity consumption for grinding the cement, translating into about 4% of the anthropogenic planet's global warming.<sup>2</sup> Hence, a key research and innovation driving effort in cement chemistry is to lower the CO<sub>2</sub> footprint.<sup>3,4</sup> In order to address this reduction, new cements based on ye'elimite, Ca<sub>4</sub>Al<sub>6</sub>O<sub>12</sub>(SO<sub>4</sub>), are being proposed to replace OPC. The main alternatives are: i) Calcium SulfoAluminate, CSA,<sup>5-7</sup> where ye'elimite content is higher than 50 wt%; ii) Belite-Ye'elimite-Ferrite cements, BYF,<sup>3,5,9</sup> where the contents are close to 60, 20, 20 wt%, respectively; and iii) Ternesite-Ye'elimite-Belite, TYB,<sup>10,11</sup> where the contents are approximately 50, 25, 20 wt%, respectively. These three materials are termed eco-cements because their manufacturing processes decrease CO<sub>2</sub> emissions, when compared to OPC (type CEM-I), by approximately 40, 25 and 25% for CSA, BYF and TYB, respectively.<sup>5,10</sup> In these cements, ye'elimite is the key phase since it develops early mechanical strengths due to the formation of the corresponding hydrated products. Ye'elimite hydrates quite fast and most of the hydration heat is released during the first 12 h. Thus, retarders may be needed to ensure the workability of the corresponding mortars and concretes.<sup>12</sup> The hydration reaction of ye'elimite in presence of a sulfate source has been reported<sup>13,14</sup> and it is shown in reaction [1], where the products are crystalline ettringite, Ca<sub>6</sub>Al<sub>2</sub>(OH)<sub>12</sub>(SO<sub>4</sub>)<sub>3</sub>·26H<sub>2</sub>O (also known as AFt), and amorphous aluminum hydroxide (also known as aluminum hydroxide gel, A-H gel or amorphous gibbsite).



The hydration reaction of ye'elimite in absence of additional sulfate sources has also been reported and it is displayed in reaction [2], where the products are crystalline calcium aluminum monosulfate,

$\text{Ca}_4\text{Al}_2(\text{OH})_{12}(\text{SO}_4)\cdot 6\text{H}_2\text{O}$  (also known as AFm) and A-H gel.<sup>13</sup> However, the reactivity of ye'elimite under these conditions is still not fully understood. Some researchers published that only reaction [2] takes place<sup>13</sup> whereas others have reported that mixtures of AFm and AFt phases are formed.<sup>15</sup>



Aluminum hydroxide gel is difficult to study because of its amorphous or poorly crystalline nature. Its presence in the pastes can be inferred from X-ray Powder Diffraction (XRPD) as some broad signals are displayed close to the positions of the diffraction peaks expected for gibbsite.<sup>13,16,17</sup> Thermo-gravimetric analysis (TGA) can also show the presence of this gel<sup>8,9,13,16-22</sup> as evidenced by the characteristic weight loss in the 250 to 280°C interval. A-H gel has also been studied using scanning electron microscopy (SEM),<sup>9,12,16,18-20</sup> and <sup>27</sup>Al magic-angle-spinning nuclear-magnetic-resonance, MAS-NMR.<sup>19,23</sup> Furthermore, a recent publication has been focused on the A-H gel characterization by SEM and transmission electron microscopy (TEM) among other techniques.<sup>16</sup> The SEM study of the gel within a CSA paste showed spherical aggregates with sizes close to 5 µm. Energy dispersive X-ray spectroscopy (EDS) data indicated a small unquantified amount of Ca.<sup>16</sup> Additional TEM/EDS characterization indicated that the A-H gel may possibly nucleate on hydrogarnet,  $\text{Ca}_3\text{Al}_2(\text{OH})_{12}$ , nanocrystals. Finally, authors in two publications<sup>18,19</sup> have speculated that A-H gels could have additional hydration water. A very recent publication,<sup>24</sup> has employed a multi-technique approach (in-situ XRPD, NMR, thermodynamic modeling and TGA) for studying the water content in hydrated aluminum hydroxide formed in the early hydration of ye'elimite with gypsum. It has been reported that the bound water content of freshly precipitated A-H gel is by far higher than expected and that a fraction is released over time, i.e. mainly during the first 24 hours of hydration. This is in contrast to the calcium silicate hydrate (C-S-H) gel in OPCs whose Ca/Si ratio, hydration degree, density and microstructure have been studied in many publications.<sup>25-29</sup>

In addition, X-ray computed tomography has become an important tool for investigating Portland cement hydration to study the pore network, tortuosity and other relevant parameters.<sup>30,31</sup> One X-ray absorption tomographic study focused on the characterization of CSA pastes has been reported.<sup>32</sup> As of today, these tomographic investigations have limited spatial resolution (usually 500 nm at best) and it is extremely difficult to distinguish between hydrated phases as the X-ray absorption of these phases are very similar. A review about the use of synchrotron radiation to investigate cements has been recently reported including an overview of the available imaging approaches.<sup>33</sup>

The state-of-the-art evolution of these imaging techniques brings to ptychographic X-ray computed tomography (PXCT), which is a scanning technique that makes use of the coherent properties of synchrotron radiation.<sup>34</sup> In coherent diffraction imaging, the post-sample X-ray optics is replaced by phase retrieval algorithms which, combined with the ptychographic approach, make PXCT robust and reliable.<sup>34-38</sup> A confined X-ray beam is used to illuminate the sample and coherent diffraction patterns are recorded in the far field from different overlapping illumination areas of the sample. The redundancy in the data and the use of iterative phase retrieval algorithms allow obtaining both the amplitude and the phase of the complex-valued transmissivity of the sample. This technique provides 2D high-resolution projections of the sample. In combination with tomography, a three-dimensional distribution of the difference from one of the real part of the refractive index,  $\delta(\mathbf{r})$ , and the imaginary part of the refractive index,  $\beta(\mathbf{r})$ , are simultaneously obtained. Thus, the complete complex-valued refractive index of the sample,  $n(\mathbf{r})=1-\delta(\mathbf{r})+i\beta(\mathbf{r})$ , can be obtained.<sup>29</sup> PXCT can provide isotropic 3D resolution better than 20 nm<sup>39</sup> and accurate mass density values when the stoichiometries are known,<sup>40</sup> which makes the technique highly appropriate for studying the microstructures of cement pastes.<sup>29,41</sup> The unparalleled sensitivity and selectivity of such a technique for measuring mass densities of every component within complex matrices, with a high spatial resolution are of particular interest to the studies of cement pastes. Recently, PXCT

has been applied to investigate the hydration, the composition, density and microstructure of an OPC paste.<sup>41</sup> The 3D maps of all the individual phases were segmented and their mass densities were quantitatively determined. Moreover, the densities and water contents of C-S-H gels were also determined<sup>29</sup> for an alite paste.

In this work, PXCT and laboratory techniques have been combined to distinguish between A-H gel and other hydrates, such as ettringite and calcium aluminum monosulfate, which are present in pastes derived from ye'elimite-containing eco-cements. Both water and calcium contents have also been quantified in the studied A-H gels and chiefly, the mass densities of the gels were obtained in untreated samples. The main aim of this study is the application of PXCT to characterize eco-cements and its potential for addressing difficult chemical challenges like mass density determination of the amorphous fraction.

## **MATERIALS AND METHODS**

Three different samples have been used in this study: I) Stoichiometric ye'elimite ( $\text{Ca}_4\text{Al}_6\text{SO}_{16}$ )<sup>42</sup> which contained 0.8 and 2.3 wt% of anhydrite and mayenite, respectively, as impurities. II) A mixture of ye'elimite and gypsum according to the stoichiometry of reaction [1]. The gypsum contained 1.5 wt% of  $\text{SrSO}_4$  as determined from Rietveld quantitative phase analysis. III) The CSA clinker was described elsewhere.<sup>43,44</sup> The mineralogical content of CSA clinker is: 72.3(1) wt% of  $\text{Ca}_4\text{Al}_6\text{SO}_{16}$ , 14.5(2) wt% of  $\beta\text{-Ca}_2\text{SiO}_4$ , 6.8(1) wt% of  $\text{CaTiO}_3$ , 2.5(2) wt% of  $\text{Ca}_4\text{Al}_2\text{Fe}_2\text{O}_{10}$ , 1.6(1) wt% of  $\text{MgO}$ ,  $\approx 1$  wt% of  $\text{Ca}_2\text{MgSi}_2\text{O}_7$  and  $\approx 1$  wt% of  $\text{CaSO}_4$ . The CSA cement used here was prepared by mixing CSA clinker with 25 wt% of anhydrite. The particle size distributions of final ye'elimite and gypsum samples were measured by dynamic light scattering, see Fig. S1.

Three types of pastes have been prepared and thoroughly studied: i) ye'elimite at 8 days of hydration (hereafter, ye'elimite paste), ii) ye'elimite and gypsum at 18 days of hydration (hereafter, ye'elimite-gypsum paste) and iii) CSA cement at 22 days of hydration (hereafter, CSA paste). Ye'elimite and

ye'elinite-gypsum pastes were studied as references. We highlight that these hydration reactions are quite fast, the reaction degree being larger than 95% at seven days.<sup>15</sup> Therefore, little evolution of the phase assemblages is expected after one week of hydration.

**PXCT experiments and data processing.** For PXCT experiments, the samples were loaded inside tapering quartz capillaries. They were stored at room temperature (RT) and measured at the cSAXS beamline at the Swiss Light Source, Paul Scherrer Institut, Villigen, Switzerland, using the instrument already described in a previous work.<sup>39</sup> Experimental details about the measurements can be found in the SI. The photon energy of the X-ray beam was 6.2 keV. Diffraction patterns were collected with an Eiger 500k detector placed 7.35 m downstream of the sample satisfying the ptychography sampling conditions.<sup>45,46</sup> The total acquisition time for all diffraction patterns including the time necessary for sample positioning was approximately 20 h for a full tomographic dataset. The ptychography reconstructions were carried out using the difference map algorithm<sup>37</sup> followed by a maximum likelihood refinement.<sup>47</sup> The pixel size of the reconstructed projections was 40.8 nm. The tomographic reconstructions were performed as described in the SI.<sup>48</sup> The spatial resolution of the tomograms was estimated by Fourier Shell Correlation (FSC) with a threshold based on the half-bit criterion.<sup>39,49</sup>

The 3D electron density distribution,  $n_e(\mathbf{r})$ , can be estimated as<sup>40</sup>

$$n_e(\mathbf{r}) = \frac{2\pi\delta(\mathbf{r})}{r_o\lambda^2} \quad [3]$$

where  $r_o$  is the electron radius and  $\lambda$  is the X-ray wavelength. PXCT provides quantitative information for materials of known chemical composition.<sup>40</sup> In this case, the mass density can be calculated as<sup>40</sup>

$$\rho(\mathbf{r}) = \frac{n_e(\mathbf{r})A}{N_A Z} \quad [4]$$

where  $N_A$  is Avogadro's number,  $A$  is the molar mass, and  $Z$  is the total number of electrons in the formula unit.

The linear attenuation coefficient,  $\mu$ , can be also obtained using equation [5]<sup>40</sup>

$$\mu(\mathbf{r}) = \left(\frac{4\pi}{\lambda}\right) \beta(\mathbf{r}) \quad [5]$$

The electron density, mass density and linear attenuation coefficient values have been obtained as detailed in the SI.

**Laboratory X-Ray Powder Diffraction (LXRPD) and data analysis.** LXRPD data were collected on a D8 ADVANCE (Bruker AXS) diffractometer equipped with a Johansson monochromator, using strictly monochromatic Mo-K $\alpha_1$  radiation,  $\lambda=0.7093$  Å, in transmission geometry ( $\theta/\theta$ ). Powder patterns were analyzed by using the GSAS suite of programs. Quartz was added to the samples as internal standard to determine the amorphous contents and it was chosen because it has a similar X-ray absorption coefficient.

**Thermal analysis.** ThermoGravimetric Analyses (TGA) were performed in a SDT-Q600 analyzer from TA instruments.

**Nuclear Magnetic Resonance (NMR).** <sup>27</sup>Al MAS NMR spectra were recorded on an AVANCEIII HD 600 (Bruker AXS) spectrometer.

**Electron microscopy.** The initial dry powders, see Fig. S2, and the resulting pastes (fracture cross-sections and polished surfaces) were characterized by Scanning Electron Microscopy (SEM) in a JEOL JSM-6490LV microscope. Energy dispersive spectroscopy (EDS) measurements were carried out on polished samples with the OXFORD INCA Energy 350 attachment. High-Resolution Transmission Electron Microscopy (HRTEM) measurements were taken using a FEI Talos F200X microscope outfitted with a FEI Super-X energy dispersive X-ray analysis system (EDS).

## RESULTS AND DISCUSSION

### Hydration of ye'elimite paste.

**PXCT analysis.** The hydration mechanism of ye'elimite, in the absence of gypsum, was initially investigated by PXCT. The volume of the reconstructed data set for this sample is about  $5 \times 10^4 \mu\text{m}^3$ . The nominal water-to-solid (w/s) ratio was 1.4 but, as reported previously,<sup>30,50</sup> it is hard to accurately control the w/s ratio homogeneity along the full length of small capillaries. PXCT yields two tomographic data sets: the 3D electron density distribution,  $n_e(\mathbf{r})$ , obtained from the phase projections, and the 3D distribution of the complex-part or the refraction index,  $\beta(\mathbf{r})$ , obtained from the absorption projections, see Fig. S3a. As expected, the resolution in the  $n_e(\mathbf{r})$  data set is better than that in the  $\beta(\mathbf{r})$ . The 3D spatial resolution, determined by FSC, was estimated to be 85 nm (Fig. S4a) for the  $n_e(\mathbf{r})$  data set. A vertical slice of this tomogram is shown in Fig. 1a, where four different component phases were identified based on their grey levels. Ten random regions or particles were analyzed for each phase to determine the electron densities, which were converted to mass densities by using equation [4] and they are given in Table 1. It can be observed that there is a good agreement between both measured and theoretical mass densities. The average relative error is lower than 1.8%.

An overall picture of the components can be obtained from the electron density histogram of a volume-of-interest (VOI) inside the capillary, see Fig. S5, of about  $4 \times 10^3 \mu\text{m}^3$  (Fig. 2a). The shift in the air peak is due to partial volume effects because the air porosity is composed of small pores below the image resolution. This plot is displayed in logarithmic scale to emphasize low content components. A similar plot, in linear scale, is given in the SI (Fig. S6a). The theoretical w/s ratio according to reaction [1] is 0.64. Therefore, the w/s ratio of 1.4, used in this work, should result in a large amount of water porosity. As it is evident in the histogram, the water porosity in this sample is negligible indicating that the w/s ratio within the scanned capillary volume is smaller than 1.4. The peaks located at  $n_e = 0.563(5) \text{ e}^- \cdot \text{\AA}^{-3}$  and  $n_e = 0.770(4) \text{ e}^- \cdot \text{\AA}^{-3}$  are due to AFt and unreacted ye'elimite, respectively, see Fig. 2a and Table 1. The contributions from AFm and A-H gel are overlapped within the strongest peak at  $n_e \approx 0.61 \text{ e}^- \cdot \text{\AA}^{-3}$ . A first

conclusion can be drawn: reactions [1] and [2] took place in agreement with the LXRPD study, described below and in a previous work.<sup>15</sup> The main peak at  $n_e \approx 0.61 \text{ e}^- \cdot \text{\AA}^{-3}$  has two contributions and this is evident in the bivariate histogram where the number of voxels is plotted as a function of both  $\delta$  (related to  $n_e$  through Eq. [4]) and  $\beta$  values, see Fig. 3a. The component phase with the larger electron density has the smaller absorption value, and thus it is identified as the aluminum hydroxide gel. Therefore, AFm has  $n_e = 0.605(5) \text{ e}^- \cdot \text{\AA}^{-3}$  and the A-H gel has  $n_e = 0.632(8) \text{ e}^- \cdot \text{\AA}^{-3}$ , see Table 1. The mass density determination of the A-H gel requires the knowledge of its composition and, hence, it will be tackled at the end of this section. The absorption tomograms are noisy, see Fig. S3, and this produces a large distribution of gray values. For materials with low absorption, some voxels have negative values (see Fig. 3) due to this noise, which has no physical significance.

Threshold-based image segmentation was performed for a large VOI of about  $3.5 \times 10^4 \mu\text{m}^3$  of the electron density tomogram and the volume of five component phases were quantified, see Table 2. The main components were A-H gel, AFm and AFt with the volume percentages being 45.7, 37.5 and 12.2 vol%, respectively. The particles sizes of the A-H gel are very small,  $\approx 5 \text{ nm}$  (see Fig. S7), which is much lower than our spatial resolution, 85 nm. Therefore, the segmented A-H gel volume refers to the A-H gel agglomerates, averaged within the resolution volume of  $(85 \text{ nm})^3$ , including any possible intermixing. Due to the difficulty of distinguishing AFm and A-H gel in the electron density tomogram, the  $\beta(\mathbf{r})$  data set was also used for the segmentation of these two phases. A cut of the 3D segmented tomogram is shown in Fig. 4a. The theoretical vol% of the hydrated phases, see Table 2, was calculated using reaction [2] as described in the SI. Table 2 displays the volume fractions obtained by PXCT, Rietveld Quantitative Phase Analysis (RQPA) and the theoretical values assuming a full chemical reaction, the latter being an approximation, as AFt is also formed.

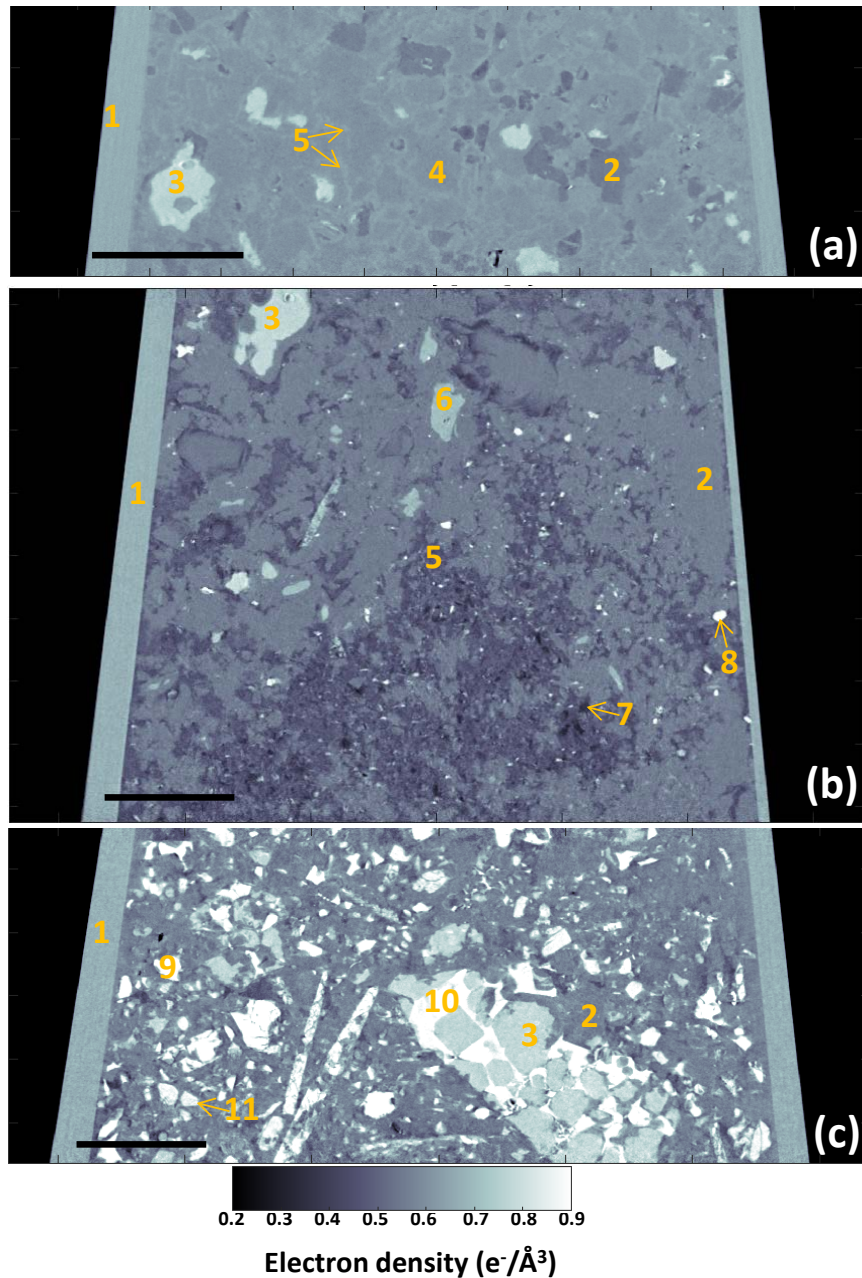


**Figure 1.** Vertical slices of the electron density tomograms from PXCT for (a) ye'elimite paste at 8 days of hydration; (b) ye'elimite-gypsum paste at 18 days of hydration; (c) CSA paste at 21 days of hydration. The different phases have been labeled: (1) capillary, (2) AFt, (3) ye'elimite, (4) AFm, (5) A-H gel, (6) gypsum, (7) free water, (8) SrSO<sub>4</sub>, (9) MgO, (10) Ca<sub>2</sub>SiO<sub>4</sub> and (11) CaSO<sub>4</sub>. Scale bar = 10 μm.

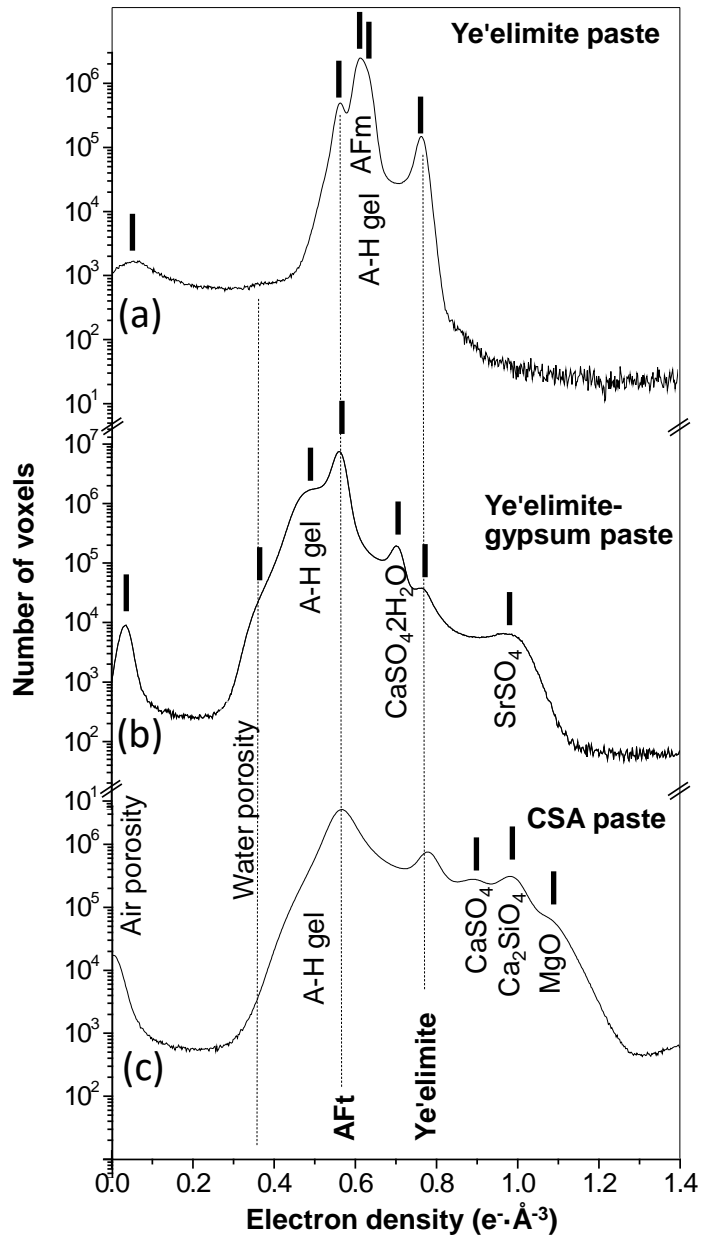


**Figure 2.** Volume-of-interest histogram of the electron densities in a logarithmic scale for (a) ye'elimite paste; (b) ye'elimite-gypsum paste; (c) CSA paste.

**Laboratory analysis.** The ye'elimite paste has been studied through laboratory techniques for a better characterization of the A-H gel. Initially, the ye'elimite-gypsum paste was prepared with a water-to-solid ratio of 1.4 which was the nominal ratio used in the PXCT study. Rietveld analysis of LXRPD data with

an internal standard allows quantifying the phase assemblage including the amorphous content. This content, for a sample where free water was removed, using a stopped-hydration methodology<sup>43</sup>, should mainly correspond to the A-H gel. However the water content of the gel under these conditions, after stopping hydration, is not necessarily the same than that determined in the PXCT characterization where there is no sample treatment. Table 2 reports the component phase contents, determined by LXRPD, transformed to volume ratios, see also Fig. 5a. It is assumed that all amorphous phase determined by LXRPD is AH-gel. The powder pattern of the ye'elimite paste shows slightly narrower gibbsite diffraction peaks, see inset in Fig. 5a, than other pastes, see below.

For the employed w/s mass ratio, 1.4, the free water content was 19.3 wt%, determined from the difference between the added water and the total water determined from TGA for the stopped-hydration sample (Fig. S8a, right panels). An additional TGA study was also performed for the non-stopped hydration paste to compare its measured weight loss, 57.4 wt%, (Fig. S8a, left panel) with the overall amount of added water, 58.3 wt%. These two values match well, validating the laboratory hydration protocol. The presence of a mixture of AFt and AFm precludes the calculation of the water content of the gel from laboratory data.

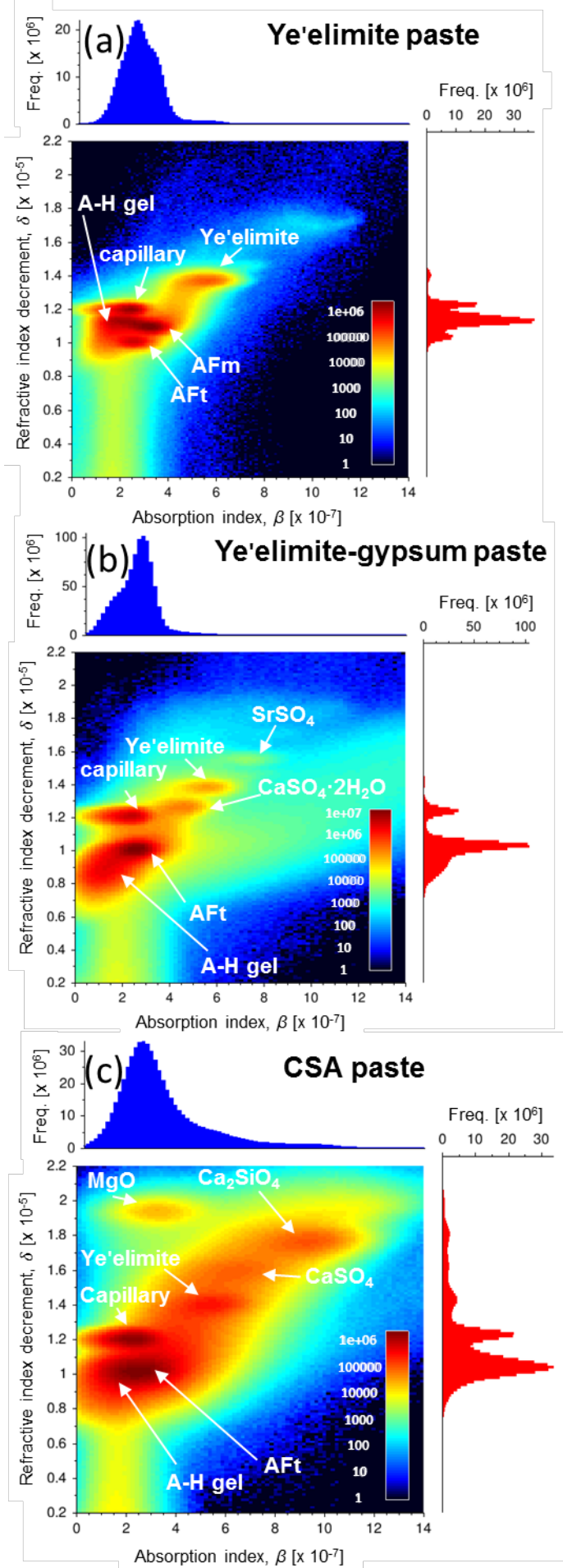


**Figure 3.** Bivariate histograms of absorption indexes ( $\beta$ ) and refractive index decrements ( $\delta$ ) for (a) ye'elimite paste; (b) ye'elimite-gypsum paste; (c) CSA paste. The peaks arising from the different components have been labeled.

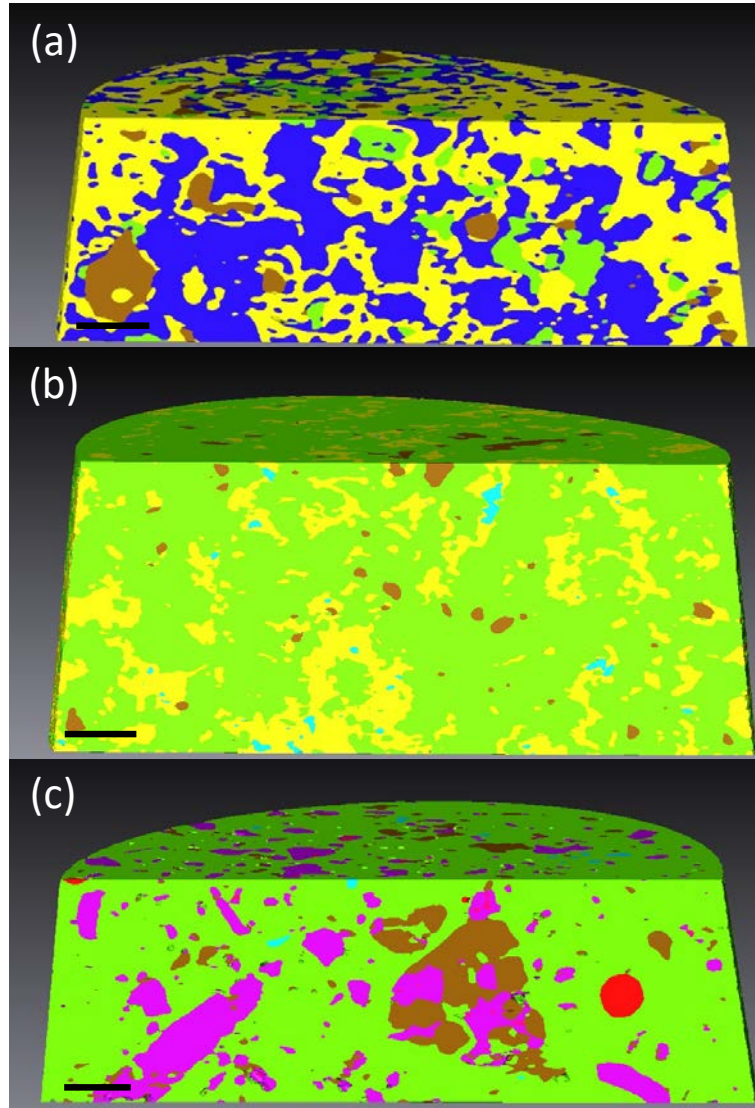


**Figure 4.** 3D renderings of the segmented volumes showing the components for (a) ye'elimite paste; (b) ye'elimite-gypsum paste; (c) CSA paste. Color codes: for hydrated phases, dark blue-AFm, green-AFt, yellow-A-H gel; for anhydrous phases, brown-ye'elimite (and gypsum), purple- $\text{Ca}_2\text{SiO}_4$ , pink-MgO; for

porosity, light blue-water porosity, red-air. For CSA paste, AFt and A-H gel are segmented together (green). Scale bar = 5 $\mu$ m.

An electron microscopy study has also been carried out to characterize the morphology of the A-H gel particles and their calcium contents.<sup>16</sup> A SEM micrograph (fracture cross-section) of the ye'elimite paste is shown in Fig. S7a. However, reliable calcium content could not be extracted from the SEM-EDS study. Therefore a HRTEM-EDS study was undertaken to estimate the possible calcium contents see Fig. S7c-e. Three samples were prepared with variable w/s ratios of 0.65, 0.77 and 1.4. From about 15 analyses per sample, the estimated average calcium-to-aluminum atomic ratios were 0.12, 0.10 and 0.06, respectively. The sulfur element contents were always lower than 1 atomic%. So we suppose that the Ca/Al ratio in the A-H gel slightly depends upon the w/s ratio with a composition close to  $(\text{CaO})_{0.12}\text{Al}(\text{OH})_3$  for a sample without free water. The calcium contents within the A-H gel agglomerates likely come from the intermixing<sup>16</sup> of  $\text{Ca}_3\text{Al}_2(\text{OH})_{12}$  and other calcium aluminate hydrates including AFm.

Additionally, the <sup>27</sup>Al MAS-NMR spectrum for the paste with w/s=1.4, see Fig. 6a, shows two bands. The low-intensity sharp band at 13.3 ppm corresponds to the aluminum in ettringite, as previously reported.<sup>20,23,52</sup> The large broader band is composed of two resonances centered at 10.2 and 9.5 ppm. The resonance at 10.2 ppm, of slightly lower intensity, corresponds to the aluminum in the AFm phase.<sup>20,23</sup> The resonance located at 9.5 ppm is likely due to the aluminum present in the A-H gel.<sup>53</sup> This resonance for crystalline gibbsite has been reported at 9.3 ppm.<sup>52,53</sup>

***A-H gel water and density determination.*** The chemical composition of the A-H gel must be known to determine the mass density from the PXCT data. For this purpose, the water content can be estimated from the PXCT data, using the  $\beta$  and  $n_e$  values, as previously reported<sup>29</sup> and detailed in the SI.

It is important to point out that the  $\beta$  values determined from the segmentation procedure were affected by the partial-volume effect, partly due to the poorer quality of the absorption tomograms. The

misdetermination in the absorption index values was minimized as follows. The 3D segmented masks of the component phases based on the  $\delta(\mathbf{r})$  tomograms were treated consecutively six times in Avizo® using Shrink/Volume tool in the Segmentation Editor. This tool applies morphological erosion of the mask using a structural element that includes the voxel of origin and its 6-connected neighbor voxels.

For estimating the water content, the calcium amount within the A-H gel must be known. The HRTEM-EDS Ca-to-Al measured value,  $(\text{CaO})_{0.12}\text{Al}(\text{OH})_3$ , was used for the calculation as it corresponds to a sample without free water, see Fig. 2a. Following this methodology,<sup>29</sup> the water stoichiometry determined for the gel,  $(\text{CaO})_{0.12}\text{Al}(\text{OH})_3.n\text{H}_2\text{O}$ , was  $-0.2\text{H}_2\text{O}$ . This water content has no physical meaning and we justify this result by the experimental uncertainties such as the errors associated to the measurements (i.e. due to low signal to noise ratio); and the possible fine intermixing of calcium aluminate hydrate (and ettringite) phases with the studied A-H gel agglomerates, which does not allow a complete separation between the component phases. Furthermore, a slightly larger calcium content within the gel aggregates,  $(\text{CaO})_{0.14}$  would yield a calculated water content of 0.0. Hence, the PXCT result indicates that the water amount of this gel, if any, is very small. Therefore, the composition of the poorly crystalline A-H gel was estimated to be  $(\text{CaO})_{0.12}\text{Al}(\text{OH})_3$ , leading to a density of  $2.05(3) \text{ g}\cdot\text{cm}^{-3}$ . Note that this value is lower than that for crystalline gibbsite, which is  $2.40 \text{ g}\cdot\text{cm}^{-3}$ .

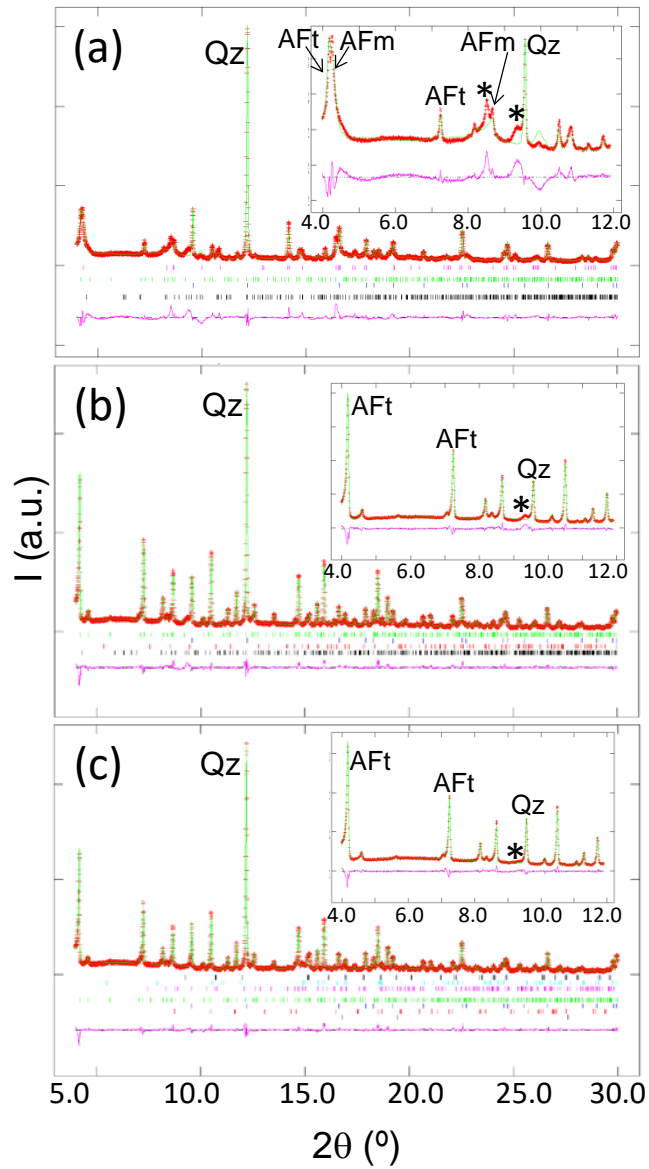


**Figure 5.** Mo- $K\alpha_1$  LXRPD Rietveld plots for (a) ye'elimitite paste at 8 days of hydration; (b) ye'elimitite-gypsum paste at 18 days of hydration; (c) CSA paste at 22 days of hydration. The tic marks are the allowed Bragg reflections. The insets show an enlarged view of the low angle region where the humps from amorphous aluminum hydroxide are highlighted with an asterisk. Qz denotes the internal standard, quartz.

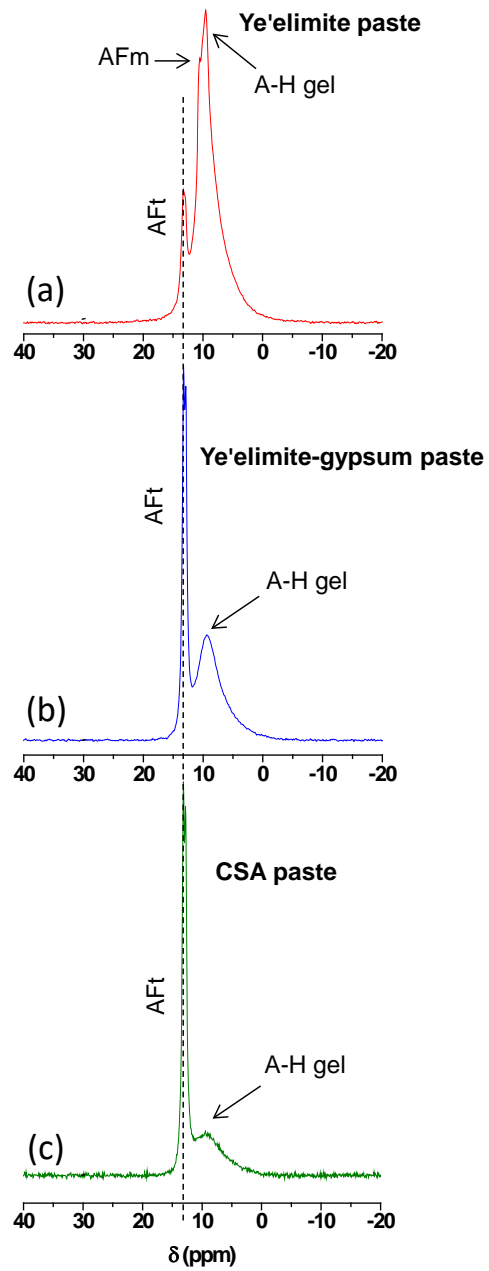


**Figure 6.**  $^{27}\text{Al}$  MAS-NMR spectra measured at a spinning rate of 15 kHz and a magnetic field of 14.1 T for (a) ye'elimite paste; (b) ye'elimite-gypsum paste; (c) CSA paste.

**Hydration of ye'elimite-gypsum paste.**

**PXCT analysis.** The ye'elimite-gypsum paste was characterized by PXCT and the volume of the reconstructed data sets for  $n_e(\mathbf{r})$  and  $\beta(\mathbf{r})$  was  $10^5 \mu\text{m}^3$ . The 3D spatial resolution of the phase tomogram obtained by FSC for  $n_e(\mathbf{r})$  was estimated to be 140 nm as shown in Fig. S4b in the SI, which is a resolution lower than that for the previous sample and consistent with the number of projections recorded. A vertical slice of the  $n_e(\mathbf{r})$  tomogram is shown in Fig. 1b. All component phases were identified, where more than ten particles of each component phase were evaluated to determine their electron densities. The mass densities shown in Table 1 match well with the theoretical values obtained from the crystallographic studies, and the average relative error is smaller than 1.0%. An overall picture of the component assemblage can be obtained from the electron density histogram of a VOI inside the capillary of about  $1.4 \times 10^4 \mu\text{m}^3$ , see Fig. 2b. Again, a shift in the air peak can be observed due to partial volume effects.

In full agreement with reaction [1], AFt is the main (crystalline) phase found in this sample,  $n_e=0.558(7) \text{ e} \cdot \text{\AA}^{-3}$ , and the second one is amorphous A-H gel,  $n_e=0.47(1) \text{ e} \cdot \text{\AA}^{-3}$ . Moreover, minor amounts of gypsum and anhydrous phases were also found. The bivariate histogram of the absorption indexes in combination with the refractive index decrements can be created and is informative for the analysis described here, see Fig. 3b. These plots are key to correctly assign the component phase in the phase contrast images as the absorption gives additional information. For instance, for partially overlapping AFt and A-H gel phases, the particles with lower electron densities have the lowest absorption  $\beta$ -values (Fig. 3b), clearly pointing towards aluminum hydroxide, see Table 1. The mass density determination of this A-H gel will be again treated at the end of the section. The different electron densities values, 0.63 and 0.47  $\text{e}/\text{\AA}^3$ , for the two investigated A-H gels are justified by their different chemical compositions, see below.

Threshold-based image segmentation was performed on a large volume of interest ( $4.6 \times 10^4 \mu\text{m}^3$ ) of the  $n_e(\mathbf{r})$  data set allowing to selectively extracting the volume occupied by every component. Five types of regions were identified and quantified and they are reported in Table 2. The main components were AFt

and A-H gel with 69.7 and 25.4 vol%, respectively. A cut of the 3D segmented tomogram is shown in Fig. 4b. The segmented value for A-H gel, 25.4 vol%, is consistent with a hydrated gel and it does not support the possibility of having amorphous anhydrous aluminum hydroxide, as this would lead to a lower volume ratio. As discussed previously, the segmented A-H gel volume refers to the A-H gel agglomerates, averaged within the resolution volume of  $(140 \text{ nm})^3$ , including any intermixing. The theoretical vol% of the hydrated phases, see Table 1, was calculated using reaction [1] but replacing  $\text{Al}(\text{OH})_3$  by  $\text{Al}(\text{OH})_3 \cdot n\text{H}_2\text{O}$  with  $n = 2.3$  as determined in the next section. The A-H gel content derived from RQPA, 39.7 vol%, is likely overestimated as it must contain any additional amorphous phase. Conversely, the A-H gel content determined from PXCT, 25.4 vol%, is likely underestimated as its fraction with higher electron density is computed by our segmentation approach as ettringite due to their similar electron density values. The theoretical expected value for A-H gel content, 33.1 vol%, lies in between.

**Laboratory analysis.** The ye'elimite-gypsum paste ( $w/s=1.4$  at 18 days of hydration) has also been studied through laboratory techniques. Table 2 reports the phase contents, determined by LXRPD, transformed to volume ratios, see Fig. 5b. To calculate the volume percentages, the density of A-H gel obtained by PXCT, detailed below, was used. The free water content was obtained as detailed before for ye'elimite paste (Fig. S8b – left and right panels).

Two main components, ettringite as rod micron particles and aluminum hydroxide gel as irregular submicron particles can be observed in the SEM micrograph of the ye'elimite-gypsum paste (fracture cross-section, Fig. S7b). All attempts to quantify the elemental composition of the A-H gel from SEM-EDS (both polished and fresh fracture surfaces) were unsuccessful. Hence, a HRTEM-EDS study was undertaken (Fig. S7f) and the chemical analysis from EDS estimated a calcium-to-aluminum atomic ratio of 0.036 for the sample hydrated in the laboratory at  $w/s$  ratio of 1.4. This value was the average of 11 analyses of selected areas having sulfur atomic contents lower than 1%. In addition, the  $^{27}\text{Al}$  MAS-NMR

spectrum for the ye'elinite-gypsum paste, see Fig. 6b, shows two bands, these resonances being due to octahedrally coordinated  $\text{Al}^{3+}$  species. The sharp band centered at 13.1 ppm is due to the aluminum in ettringite. A second broad single band is centered at 9.4 ppm. This resonance is likely due to the aluminum within the A-H gel and it has been previously reported between 11.5 and 7.5 ppm for amorphous aluminum hydroxides<sup>53</sup> and very close to the reported value for crystalline gibbsite, 9.3 ppm.<sup>52,53</sup>

**A-H gel water and density determination.** The calcium content of the A-H gel estimated from the HRTEM-EDS study is close to  $(\text{CaO})_{0.04}\text{Al}(\text{OH})_3$ . The water content can be estimated from the PXCT data, using the  $\beta$  and  $n_e$  values, as described above and detailed in the SI. Following this methodology,<sup>29</sup> the water stoichiometry determined for the gel,  $(\text{CaO})_{0.04}\text{Al}(\text{OH})_3 \cdot n\text{H}_2\text{O}$ , was  $2.3\text{H}_2\text{O}$ , leading to a gel density value of  $1.48(3) \text{ g}\cdot\text{cm}^{-3}$ , see Table 1. The degree of hydration and calcium content modify the mass density in a minor way. The mass density of this component assuming a composition of  $\text{Al}(\text{OH})_3$  would be  $1.53 \text{ g}\cdot\text{cm}^{-3}$ .

Taking all the characterization together, the A-H gel micrometer-size agglomerates for ye'elinite-gypsum paste has a composition close to  $(\text{CaO})_{0.04}\text{Al}(\text{OH})_3 \cdot 2.3\text{H}_2\text{O}$ , with electron and mass density values of  $0.47 \text{ e}/\text{\AA}^3$  and  $1.48 \text{ g}\cdot\text{cm}^{-3}$ , respectively. Conversely, the composition of the A-H gel agglomerates for the ye'elinite paste is close to  $(\text{CaO})_{0.12}\text{Al}(\text{OH})_3$ , with electron and mass density values of  $0.63 \text{ e}/\text{\AA}^3$  and  $2.05 \text{ g}\cdot\text{cm}^{-3}$ , respectively.

### **Hydration of CSA paste.**

**PXCT analysis.** The volume of the reconstructed data sets for the CSA paste was about  $7.5 \times 10^4 \mu\text{m}^3$ . The 3D spatial resolution of the  $n_e(\mathbf{r})$  phase tomogram obtained by FSC was estimated as 133 nm, see Fig S4c. A vertical slice of the phase contrast tomogram is shown in Fig. 1c. Selected VOIs were analyzed to obtain the electron densities of the phases and subsequently the mass densities, see Table 1. Theoretical mass densities and mass attenuation coefficients are also reported for the sake of comparison. Although the

CSA is a quite complex sample, the calculated mass densities matched well with the theoretical densities. An overall picture of the phase assemblage can be obtained from the  $n_e$  histogram of a VOI of about  $1.4 \times 10^4 \mu\text{m}^3$ , see Fig. 2c. Some anhydrous phases appear poorly resolved in the histogram but they could be identified using the information available in the bivariate histogram, see Fig. 3c. Even component phases with low contents, smaller than 0.5 vol%, such as anhydrite or MgO, could be easily identified. According to reaction [1], AFt is the main hydrated phase in this paste as the cement contained soluble sulfates. No clear  $n_e$  peak from A-H gel was found in the histogram, see Fig. 2c. Furthermore, the bivariate plot, see Fig. 3c, does not show a distinct contribution from this phase. However, the TGA measurement, shown in Fig. S8c, clearly shows the presence of A-H gel. Moreover, the  $^{27}\text{Al}$  MAS-NMR spectrum in Fig. 6c also conspicuously shows the signature of A-H gel. We therefore conclude that the contribution of the gel is hindered within the large contribution of ettringite in the  $n_e(\mathbf{r})$  data set. The  $n_e$  histogram in Fig. S6c shows the values of the full width at half maximum (FWHM) of the largest peak. The FWHM value of the AFt peak in the CSA paste doubles those of AFt in ye'elimite-gypsum and ye'elimite pastes. This could be explained by the density of the A-H gel being close to  $1.5 \text{ g}\cdot\text{cm}^{-3}$ , so that its  $n_e$  signal in the histogram is masked by the AFt strong contribution. The difficulty to separate the two hydrated phases precludes an accurate determination of the water content and mass density for this A-H gel.

Threshold-based image segmentation was also carried out, see Table 2, for a volume of about  $4.5 \times 10^4 \mu\text{m}^3$ . The sample contained: 74.3 vol% of hydrated phases: AFt and A-H gel; 11.3 vol% of unreacted ye'elimite; 13.6 vol% of belite and other minor phases. Belite hydration has not been observed. This is in agreement with a previous work that it showed that belite hydration started after 28 days of hydration for this type of CSA cements.<sup>43</sup> However this is in discrepancy with belite hydration in Portland cement that it starts earlier. A cut of the 3D segmented tomogram is shown in Fig. 4c. The relatively high content of unreacted ye'elimite measured by PXCT means that the w/s ratio in the scanned part of the capillary was

smaller than the nominal value of 1.4. In the laboratory study, where homogeneity is ensured by the hydration protocol, ye'elimite was not observed, see Table 2. The accuracy of the reconstructions and segmentations is ensured by the measured MgO content. CSA anhydrous cement had 1.2 wt% of MgO which does not hydrate under the reported conditions. The MgO content in volume percentage after water dilution should be 0.2 vol%, which agrees with the measured values in the paste by PXCT and LXRPD, 0.3 vol%, see Table 2. Although no much new information is attained here, this study supports the results obtained for the ye'elimite-gypsum sample study.

**Laboratory analysis.** CSA has also been studied by LXRPD in combination with the Rietveld method to determine the component phase assemblage. Table 2 reports its RQPA transformed to volume ratios, see also Fig. 5c. The density of A-H gel obtained in the ye'elimite-gypsum paste,  $1.48 \text{ g}\cdot\text{cm}^{-3}$ , was used for this calculation. Fig. S8c reports the TGA traces for both the non-stopped and stopped-hydration pastes. The  $^{27}\text{Al}$  MAS-NMR spectrum for the CSA paste, Fig. 6c, contains two bands with different widths. The sharp intense band centered at 13.0 ppm is due to the aluminum in ettringite as discussed previously. The low-intensity broad band centered at 9.3 ppm is due to the aluminum within the A-H gel which could not be disentangled in the tomographic study.

## CONCLUSIONS

The water content and the calcium uptake of aluminum hydroxide gels in ye'elimite eco-cements have been established, with Ca contents being minor but not negligible. Using a combination of ptychographic X-ray computed tomography (PXCT), which provides 3D distributions of the electron density,  $n_e(\mathbf{r})$ , and the complex part of the refractive index,  $\beta(\mathbf{r})$ , within the specimens, and laboratory techniques, we could shed light to open questions in the chemistry of these eco-cement pastes. Bivariate plots of  $n_e$  and  $\beta$  values have allowed distinguishing between component phases with similar electron densities, such as aluminum hydroxide gel and calcium aluminum monosulfate. In addition to image the cement paste components,

the aluminum hydroxide gel densities have been determined for different gel compositions. A gel with high water content,  $(\text{CaO})_{0.04}\text{Al}(\text{OH})_3 \cdot 2.3\text{H}_2\text{O}$ , has a density of  $1.48 \text{ g}\cdot\text{cm}^{-3}$ . Conversely, a gel without significant water content,  $(\text{CaO})_{0.12}\text{Al}(\text{OH})_3$  has much higher density,  $2.05 \text{ g}\cdot\text{cm}^{-3}$ . In any case these densities are lower than that of crystalline gibbsite,  $2.40 \text{ g}\cdot\text{cm}^{-3}$ . Additionally, the density of an aluminum hydroxide gel present in a calcium sulfoaluminate commercial cement paste has been estimated to be close to  $1.5 \text{ g}\cdot\text{cm}^{-3}$ . Moreover, the volume ratio of different material phases, quantitatively determined from PXCT data agrees well with the results obtained from laboratory measurements. It must also be noted that  $^{27}\text{Al}$  MAS-NMR studies allowed detecting every phase containing aluminum.

## **ASSOCIATED CONTENT**

### **Supporting Information.**

Additional details for Materials and Methods section. Further features of the ptychographic X-ray computed tomography experiments and data processing are also given. Mass and volume data for the two chemical reactions are provided. Finally, Figures S1 to S8 give further details about the laboratory and synchrotron characterization of the samples.

## **AUTHOR INFORMATION**

**Corresponding Author:** \*migarcia@cells.es

### **Author Contributions**

M.A.G.A. designed the research; A.C. and P.T. did sample preparations for the PXCT study; A.C., A.G.D.T and I.S. performed laboratory research; A.C., P.T., J.d.S, A.D. and M.H. performed PXCT measurements and data analysis; A.C. and M.A.G.A. wrote a draft of the manuscript which was upgraded with the participation of all the authors.

## Funding Sources

This work has been supported by MINECO through BIA2014-57658-C2-1-R and BIA2014-57658-C2-2-R, which is co-funded by FEDER, research grants. We thank SLS for providing beamtime at the cSAXS beamline. We also thank the Swiss National Science Foundation SNF for the support to the work of J. C. da Silva (Grant No. 137772). Instrumentation development was supported by SNF (R'EQUIP, No. 145056, "OMNY") and the Competence Centre for Materials Science and Technology (CCMX) of the ETH-Board, Switzerland. In addition, the authors would like to thank Dr. Manuel Guizar-Sicairos for his valuable assistance with the ptychography and PXCT data analysis.

## REFERENCES

- (1) Kurtis, K. E. Innovations in Cement-Based Materials: Addressing Sustainability in Structural and Infrastructure Applications. *MRS Bull.* **2015**, *40*, 1102-1108.
- (2) McCaffrey, R. Climate change and the cement industry. *Global Cement and Lime Magazine Environmental Special Issue*, **2002**, 15-19.
- (3) Barcelo, L.; Kline, J.; Walenta, G.; Gartner, E. Cement and Carbon Emissions. *Mater. Struct.* **2014**, *47*, 1055-1065.
- (4) Gartner, E.; Hirao, H. A Review of Alternative Approaches to the Reduction of CO<sub>2</sub> Emissions Associated with the Manufacture of the Binder Phase in Concrete. *Cem. Concr. Res.* **2015**, *78*, 126-142.
- (5) Aranda, M. A. G.; De la Torre, A. G. Sulfoaluminate Cement. In *Eco-efficient Concrete*; Pacheco-Torgal, F., Jalali, S., Labrincha, J, Eds.; Woodhead Publishing: Cambridge, 2013; pp. 488-522.
- (6) Zhang, L.; Su, M.; Wang, Y. Development of the use of sulfo- and ferroaluminate cements in China. *Adv. Cem. Res.* **1999**, *11*, 15-21.

- (7) Mehta, P. K. Investigations on energy-saving cements. *World Cem. Technol.* **1980**, *11*, 166–177
- (8) Álvarez-Pinazo, G.; Santacruz, I.; León-Reina, L.; Aranda, M. A. G.; De la Torre, A. G. Hydration Reactions and Mechanical Strength Developments of Iron-Rich Sulfoelite Eco-cement. *Ind. Eng. Chem. Res.* **2013**, *52*, 16606-16614.
- (9) Chen, I. A.; Hargis, C. W.; Juenger, M. C. G. Understanding Expansion in Calcium Sulfoaluminate–Belite Cements. *Cem. Concr. Res.* **2012**, *42*, 51-60.
- (10) Bullerjahn, F.; Schmitt, D.; Ben Haha, M. Effect of Raw Mix Design and of Clinkering Process on the Formation and Mineralogical Composition of (Ternesite) Belite Calcium Sulphoaluminate Ferrite Clinker. *Cem. Concr. Res.* **2014**, *59*, 87-95.
- (11) Shen, Y.; Qian, J.; Huang, Y.; Yang, D. Synthesis of Belite Sulfoaluminate-Ternesite Cements with Phosphogypsum. *Cem. Concr. Compos.* **2015**, *63*, 67-75.
- (12) Zajac, M.; Skocek, J.; Bullerjahn, F.; Ben Haha, M. Effect of Retarders on the Early Hydration of Calcium-Sulpho-Aluminate (CSA) Type Cements. *Cem. Concr. Res.* **2016**, *84*, 62-75.
- (13) Winnefeld, F.; Barlag, S. Calorimetric and Thermogravimetric Study on the Influence of Calcium Sulfate on the Hydration of Ye'elinite. *J. Therm. Anal. Calorim.* **2010**, *101*, 949-957.
- (14) Hargis, C. W.; Kirchheim, A. P.; Monteiro, P. J. M.; Gartner, E. M. Early age Hydration of Calcium Sulfoaluminate (Synthetic Ye'elinite,  $C_4A_3S$ ) in the Presence of Gypsum and Varying Amounts of Calcium Hydroxide. *Cem. Concr. Res.* **2013**, *48*, 105-115.
- (15) Cuesta, A.; Álvarez-Pinazo, G.; Sanfélix, S. G.; Peral, I.; Aranda, M. G. A.; De la Torre, A. G. Hydration Mechanisms of Two Polymorphs of Synthetic Ye'elinite. *Cem. Concr. Res.* **2014**, *63*, 127-136.

- (16) Song, F.; Yu, Z.; Yang, F.; Lu, Y.; Liu, Y. Microstructure of Amorphous Aluminum Hydroxide in Belite-Calcium Sulfoaluminate Cement. *Cem. Concr. Res.* **2015**, *71*, 1-6.
- (17) Bullerjahn, F.; Zajac, M.; Mohsen, B. H. CSA Raw Mix Design: Effect on Clinker Formation and Reactivity. *Mater. Struct.* **2015**, *48*, 3895-3911.
- (18) Bizzozero, J.; Gosselin, C.; Scrivener, K. L. Expansion Mechanisms in Calcium Aluminate and Sulfoaluminate Systems with Calcium Sulfate. *Cem. Concr. Res.* **2014**, *56*, 190-202.
- (19) Pelletier, L.; Winnefeld, F.; Lothenbach, B. The Ternary System Portland Cement–Calcium Sulphoaluminate Clinker–Anhydrite: Hydration Mechanism and Mortar Properties. *Cem. Concr. Compos.* **2010**, *32*, 497-507.
- (20) Allevi, S.; Marchi, M.; Scotti, F.; Bertini, S.; Cosentino, C. Hydration of Calcium Sulphoaluminate with Additions of Different Calcium Sulphate Sources. *Mater. Struct.* **2016**, *49*, 453-466.
- (21) Telesca, A.; Marroccoli, M.; Pace, M. L.; Tomasulo, M.; Valenti, G. L.; Monteiro, P. J. A Hydration Study of Various Calcium Sulfoaluminate Cements. *Cem. Concr. Compos.* **2014**, *53*, 233-238.
- (22) Pelletier-Chaignat, L.; Winnefeld, F.; Lothenbach, B.; Le Saout, G.; Müller, C. J.; Famy, C. Influence of the Calcium Sulphate Source on the Hydration Mechanism of Portland Cement-Calcium Sulphoaluminate Clinker-Calcium Sulphate Binders. *Cem. Concr. Compos.* **2011**, *33*, 551-561.
- (23) Paul, G.; Boccaleri, E.; Buzzi, L.; Canonico, F.; Gastaldi, D. Friedel's Salt Formation in Sulfoaluminate Cements: A Combined XRD and  $^{27}\text{Al}$  MAS NMR Study. *Cem. Concr. Res.* **2015**, *67*, 93-102.
- (24) Jansen, D.; Spies, A.; Neubauer, J.; Ectors, D.; Goetz-Neunhoeffler, F. Studies on the Early Hydration of Two Modifications of Ye'elimite with Gypsum, *Cem. Concr. Res.* **2017**, *91*, 106-116.
- (25) Richardson, I. G. Model Structures for C-(A)-S-H(I). *Acta Crystallogr. B* **2014**, *70*, 903-923.

- (26) Pellenq, R. J.; Kushima, A.; Shahsavari, R.; Van Vliet, K. J.; Buehler, M. J.; Yip, S.; Ulm, F. J. A Realistic Molecular Model of Cement Hydrates. *Proc. Natl. Acad. Sci. U. S. A.* **2009**, *106*, 16102–16107.
- (27) Berodier, E.; Scrivener, K. Understanding the Filler Effect on the Nucleation and Growth of C-S-H. *J. Eur. Ceram. Soc.* **2014**, *97*, 3764-3773.
- (28) Allen, A. J.; Thomas, J. J.; Jennings, H. M. Composition and Density of Nanoscale Calcium-Silicate-Hydrate in Cement. *Nat. Mater.* **2007**, *6*, 311-316.
- (29) da Silva, J. C.; Trtik, P.; Diaz, A.; Holler, M.; Guizar-Sicairos, M.; Raabe, J.; Bunk, O.; Menzel, A. Mass Density and Water Content of Saturated Never-Dried Calcium Silicate Hydrates. *Langmuir* **2015**, *31*, 3779-3783.
- (30) Gallucci, E.; Scrivener, K.; Groso, A.; Stampanoni, M.; Margaritondo, G. 3D Experimental Investigation of the Microstructure of Cement Pastes Using Synchrotron X-ray Microtomography ( $\mu$ CT). *Cem. Concr. Res.* **2007**, *37*, 360-368.
- (31) Jackson, M. D.; Landis, E. N.; Brune, P. F.; Vitti, M.; Chen, H.; Li, Q.; Kunz, M.; Wenk, H.-R.; Monteiro, P. J. M.; Ingraffea, A. R. Mechanical Resilience and Cementitious Processes in Imperial Roman Architectural Mortar. *Proc. Natl. Acad. Sci. U. S. A.* **2014**, *111*, 18484–18489.
- (32) Gastaldi, D.; Canonico, L.; Capilli, E.; Boccaleri, M.; Milanesio, L.; Palin, G.; Croce, F.; Marone, K.; Mader, K.; Stampanoni, M. In Situ Tomographic Investigation on the Early Hydration Behaviours of Cementing Systems. *Constr. Build. Mater.* **2012**, *29*, 284-290.
- (33) Aranda, M. A. G. Recent Studies of Cements and Concretes by Synchrotron Radiation Crystallographic and Cognate Methods. *Crystallogr. Rev.* **2016**, *22*, 150-196.

- (34) Dierolf, M.; Menzel, A.; Thibault, P.; Schneider, P.; Kewish, C. M.; Wepf, R.; Bunk, O.; Pfeiffer, F. Ptychographic X-ray Computed Tomography at the Nanoscale. *Nature* **2010**, *467*, 436-440.
- (35) Rodenburg, J.; Hurst, A. C.; Cullis, A. G.; Dobson, B. R.; Pfeiffer, F.; Bunk, O.; David, C.; Jefimovs, K.; Johnson, I. Hard X-rays Lensless Imaging of Extended Objects. *Phys. Rev. Lett.* **2007**, *98*, 034801
- (36) Guizar-Sicairos, M.; Fienup, J. R. Phase Retrieval with Transverse Translation Diversity: a Nonlinear Optimization Approach. *Opt. Express* **2008**, *16*, 7264-7278.
- (37) Thibault, P.; Dierolf, M.; Bunk, O.; Menzel, A.; Pfeiffer, F. Probe Retrieval in Ptychographic Coherent Diffractive Imaging. *Ultramicroscopy* **2009**, *109*, 338-343.
- (38) Faulkner, H. M. L.; Rodenburg, J. M. Movable Aperture Lensless Transmission Microscopy: a Novel Phase Retrieval Algorithm. *Phys. Rev. Lett.* **2004**, *93*, 023903.
- (39) Holler, M.; Diaz, A.; Guizar-Sicairos, M.; Karvinen, P.; Färm, E.; Härkönen, E.; Ritala, M.; Menzel, A.; Raabe, J.; Bunk, O. X-ray Ptychographic Computed Tomography at 16 nm Isotropic 3D Resolution. *Sci. Rep.* **2014**, *4*, 3857.
- (40) Diaz, A.; Trtik, P.; Guizar-Sicairos, M.; Menzel, A.; Thibault, P.; Bunk, O. Quantitative X-ray Phase Nanotomography. *Phys. Rev. B* **2012**, *85*, 020104.
- (41) Trtik, P.; Diaz, A.; Guizar-Sicairos, M.; Menzel, A.; Bunk, O. Density Mapping of Hardened Cement Paste Using Ptychographic X-ray Computed Tomography. *Cem. Concr. Compos.* **2013**, *36*, 71-77.
- (42) Cuesta A, De la Torre, A. G.; Losilla, E. R.; Peterson, V. K.; Rejmak, P.; Ayuela, A.; Frontera, C.; Aranda, M. A. G. Structure, Atomistic Simulations, and Phase Transition of Stoichiometric Yeelimité. *Chem. Mater.* **2013**, *25*, 1680-1687.
- (43) García-Maté, M.; De la Torre, A. G.; León-Reina, L.; Aranda, M. A. G.; Santacruz, I. Hydration Study of Calcium Sulfoaluminate Cements Blended with Fly Ash. *Cem. Concr. Res.* **2013**, *54*, 12-20.

- (44) García-Maté, M.; Santacruz, I.; De la Torre, A. G.; León-Reina, L.; Aranda, M. A. G. Rheological and hydration characterization of calcium sulfoaluminate cements. *Cem. Concr. Compos.* **2012**, *34*, 684-691.
- (45) da Silva, J. C.; Menzel, A. Elementary Signals in Ptychography. *Opt. Express* **2015**, *23*, 33812-21.
- (46) Edo, T. B.; Batey, D. J.; Maiden, A. M.; Rau, C.; Wagner, U.; Pešić, Z. D.; Waigh, T. A.; Rodenburg, J. M. Sampling in X-Ray Ptychography. *Phys. Rev. A* **2013**, *87*, 053850.
- (47) Thibault, P.; Guizar-Sicairos, M. Maximum-Likelihood Refinement for Coherent Diffractive Imaging. *New J. Phys.* **2012**, *14*, 063004.
- (48) Guizar-Sicarios, M.; Diaz, A.; Holler, M.; Lucas, M. S.; Menzel, A.; Wepf, R. A.; Bunk, O. Phase Tomography from X-Ray Coherent Diffractive Imaging Projections. *Opt. Express* **2011**, *19*, 21345-21357.
- (49) Van Hell, M.; Schatz, M. Fourier Shell Correlation Threshold Criteria. *J. Struct. Biol.* **2005**, *151*, 250-262.
- (50) Parisatto, M.; Dalconi, M. C.; Valentini, L.; Artioli, G.; Rack, A.; Tucoulou, R.; Cruciani, G.; Ferrari, G. Examining Microstructural Evolution of Portland Cements by In-Situ Synchrotron Micro-Tomography. *J. Mater. Sci.* **2015**, *50*, 1805-1817.
- (51) Henke, B. L.; Gullikson, E. M.; Davis, J. C. X-Ray Interactions: Photoabsorption, Scattering, Transmission, and Reflection at  $E = 50\text{-}30,000$  eV,  $Z = 1\text{-}92$ . *At. Data Nucl. Data Tables* **1993**, *54*, 181-342.
- (52) Skibsted, J.; Henderson, E.; Jakobsen, H. J. Characterization of Calcium Aluminate Phase in Cements by  $^{27}\text{Al}$  MAS NMR Spectroscopy. *Inorg. Chem.* **1993**, *32*, 1013-1027.

(53) Isobe, T.; Watanabe, T.; d'Epinose de la Caillerie, J. B.; Legrand, A. P.; Massiot, D. Solid State  $^1\text{H}$  and  $^{27}\text{Al}$  NMR Studies of Amorphous Aluminum Hydroxides. *J. Colloid. Interface Sci.* **2003**, *261*, 320-324.

**Table 1. Electron, Mass Densities and Mass Attenuation Coefficients ( $\mu$ ) by PXCT. Expected Mass Densities Taken from the CIF Files and Expected<sup>51</sup> Mass Attenuation Coefficients ( $\mu$ )**

Phase	$n_e^{\S} / e^- \cdot \text{\AA}^{-3}$			mass density <sup>&amp;</sup> / $\text{g} \cdot \text{cm}^{-3}$			Expected mass density <sup>#</sup> / $\text{g} \cdot \text{cm}^{-3}$	$\mu^* / \text{cm}^{-1}$			Expected $\mu^{\dagger} / \text{cm}^{-1}$
	Y paste	Y-G paste	CSA paste	Y paste	Y-G paste	CSA paste		Y paste	Y-G paste	CSA paste	
ye'elimité	0.770(4)	0.770(5)	0.784(4)	2.58(1)	2.58(2)	2.64(1)	2.60	340	376	342	361.1
gypsum	-	0.704(3)	-	-	2.28(1)	-	2.30	-	274	-	300.0
AFt	0.563(5)	0.558(7)	0.569(7)	1.79(2)	1.77(2)	1.80(2)	1.78	152	172	159	181.0
AFm	0.605(5)	-	-	1.94(2)	-	-	2.02	231	-	-	247.7
A-H gel	0.632(8)	0.47(1)	-	2.05(3)	1.48(3)	-	2.40 <sup>\S</sup>	133	63	-	120.0 <sup>\S</sup>
capillary	0.670(3)	0.677(5)	0.672(3)	2.22(1)	2.25(2)	2.24(1)	2.20	160	157	156	161.8

<sup>\S</sup> Y-G paste: 0.97(3) and 0.38(3)  $e^- \cdot \text{\AA}^{-3}$  for  $\text{SrSO}_4$  and  $\text{H}_2\text{O}$ . CSA paste: 0.887(8), 0.978(8) and 1.08(3)  $e^- \cdot \text{\AA}^{-3}$  for  $\text{CaSO}_4$ ,  $\text{Ca}_2\text{SiO}_4$  and  $\text{MgO}$

<sup>&</sup> Y-G paste: 3.4(1) and 1.13(9)  $\text{g} \cdot \text{cm}^{-3}$  for  $\text{SrSO}_4$  and  $\text{H}_2\text{O}$ . CSA paste: 2.94(3), 3.25(3) and 3.6(1)  $\text{g} \cdot \text{cm}^{-3}$  for  $\text{CaSO}_4$ ,  $\text{Ca}_2\text{SiO}_4$  and  $\text{MgO}$

<sup>#</sup> Theoretical mass densities are 3.96, 1.00, 2.95, 3.30 and 3.58  $\text{g} \cdot \text{cm}^{-3}$  for  $\text{SrSO}_4$ ,  $\text{H}_2\text{O}$ ,  $\text{CaSO}_4$ ,  $\text{Ca}_2\text{SiO}_4$  and  $\text{MgO}$

<sup>\*</sup> Measured absorption coefficients in CSA paste are 603 and 213  $\text{cm}^{-1}$  for  $\text{Ca}_2\text{SiO}_4$  and  $\text{MgO}$

<sup>\dagger</sup> Theoretical absorption coefficients are 582.0, 20.9, 459.8, 621.4 and 210.8  $\text{cm}^{-1}$  for  $\text{SrSO}_4$ ,  $\text{H}_2\text{O}$ ,  $\text{CaSO}_4$ ,  $\text{Ca}_2\text{SiO}_4$  and  $\text{MgO}$

<sup>\S</sup> Values for crystalline gibbsite,  $\text{Al}(\text{OH})_3$

**Table 2. Phase Contents (Volume Percentages) Determined by LXRPD and by PXCT. Expected Phase Volume Contents Obtained from Full Chemical Reactions**

Phase	LXRPD <sup>§</sup> / vol%			PXCT <sup>&amp;</sup> / vol%			Theoretical percentage / vol%	
	Y paste	Y-G paste	CSA paste	Y paste	Y-G paste	CSA paste	Y paste	Y-G paste
ye'elimite	1.1(1)	0.3(1)	-	4.0	3.6 <sup>#</sup>	11.3	-	-
AFt	12.1(3)	59.6(1)	53.5(1)	12.2	69.7	74.3 <sup>*</sup>	-	68.6
AFm	31.9(3)	-	-	37.5	-	-	66.9	-
A-H gel	54.9(2)	39.7(1)	40.9(1)	45.7	25.4	-	33.1	31.4

<sup>§</sup> Y-G paste also contains 0.4(1) vol% of gypsum. CSA paste also contains 3.5(2), 1.0(1), 0.6(1), 0.3(1) and 0.2(1) vol% of Ca<sub>2</sub>SiO<sub>4</sub>, CaTiO<sub>3</sub>, Ca<sub>2</sub>AlFeO<sub>5</sub>, MgO, and CaSO<sub>4</sub>, respectively.

<sup>&</sup> Y paste also contains 0.6 vol% of air porosity. Y-G paste also contains 0.9 vol% and 0.4 vol% of water of air porosities, respectively. CSA paste also contains 13.6, 0.3, 0.3 and 0.2 vol% of remaining anhydrous phases (mainly Ca<sub>2</sub>SiO<sub>4</sub>), MgO, water porosity and air porosity, respectively.

<sup>#</sup>This value also includes the contribution from gypsum which could not be disentangled

<sup>\*</sup>This value also includes the contribution from A-H gel which could not be disentangled

TOC graphic:

